Figure 1: NGSIM trajectories (the color represents the measured speed of each car in m/s)

1 Numerical validation

Many phenomena interact in vehicular flow on a freeway. The ARZ equations provide a finer modelling of these dynamics. Studying of the linearized model in the spectral domain brings up a simple framework that paves the way to establishing control strategies for the system. Prior to using such techniques, it is necessary to assess how realistic the model is in its linearized form. This is the topic of this section that will confront the prediction of the model and the actual flow and velocity data gathered in the well known NGSIM data set.

1.1 Data source: NGSIM trajectories

The NSGIM trajectory data set gathers trajectories of vehicles sampled with a 10 Hz frequency thanks to high precision cameras. After converting units to the universal system, each point in the table contains several pieces of information such as **vehicle_ID** (each vehicle has a unique ID), **veh_class** (1 for motorcycle, 2 for cars, 3 for trucks, only cars are taken into account here), **time_since_epoch_ms** (time in ms since epoch timestamp), **local_y** (longitudinal coordinate of the front center of the vehicle with respect to the entry edge of the section in the direction of travel) (meters), **veh_v** (vehicle speed) (meters per second). 45 minutes are recorded on a 650 meter long section. There are five lanes along the section of the freeway under scrutiny which is taken into account when computing the lineic density of vehicles ρ. The trajectories are represented in the (t, x) domain on Figure 1.

1.2 Reconstructing (v, q) maps from NGSIM trajectories

The NGSIM does not directly provide the values $v(t, x)$ and $q(t, x)$ in the resolution domain $[0, T] \times [0, L]$. In order to obtain macroscopic quantities out of the microscopic measurements, one divides the time and space grid $[0, T] \times [0, L]$ into small buckets $([i \, \Delta t, \, (i + 1) \, \Delta t] \times [j \, \Delta x, \, (j + 1) \, \Delta x])_{i \in \{1 \dots n_t\}, j \in \{1 \dots n_x\}}$. Here i corresponds to time and j to space. The operation consists in gathering the corresponding data points into bins and then estimating the quantities of interest in each bin. Let $card$ denote the function that gives the number of elements in a given set i.e. its cardinal.

1.2.1 Binning formulae

The size of each bucket is $\Delta t \times \Delta x$. In each bucket, a certain number of traces are available and ρ, v and q are assumed to be constant. Here several formulae are presented that enable the conversion of a set of records of vehicles' positions into a map of speed, flow and density as a function of time and position.

Binning formula for v: The speed is assumed to be constant in each bucket. Thus a straightforward estimator for that quantity is the empirical average. Let $\widehat{v}_{i,j}$ the estimator for the speed in bucket (i, j).

$$\widehat{v}_{i,j} = mean_{trace \in bucket_{i,j}} \left(v \left(trace \right) \right)$$

1

Binning formula for ρ: One considers a bucket with index (i,j). by definition

$$\rho_{i,j} = \frac{1}{n_{lanes}\, \Delta x\, \Delta t} \int\int_{(t,x)\in[i\,\Delta t,\,(i+1)\,\Delta t]\times[j\,\Delta x,\,(j+1)\,\Delta t]} \rho\,(x,t)\,dxdt$$

Any given vehicle will have its position recorded every 0.1 second. Therefore it is also possible to count the number of traces in a given bucket and normalize it by the sampling rate. The contribution of a given vehicle to the density of a bucket is proportional to the number of traces it has left in the bucket. If the speed is assumed to be locally constant, this is proportional to the time this vehicle spends in the bucket and consistent with the conservation of the total number of vehicles across all buckets.

$$\widehat{\rho}_{i,j} = \frac{1}{n_{lanes}\, \Delta x\, \Delta t\, \text{sampling rate}} card\left(\{trace \mid trace \,\in\, bucket\}\right)$$

Binning formula for q: By definition, $q(x,t) = \rho(x,t)\,v(x,t)$ so a first estimator for q in the bucket (i,j) is logically

$$\widehat{q}_{i,j} = \widehat{v}_{i,j}\widehat{\rho}_{i,j}$$

One can also approximate the flux going through a given bucket $[i\,\Delta t,\,(i+1)\,\Delta t]\times[j\,\Delta x,\,(j+1)\,\Delta t]$ by the number of cars crossing the x coordinate $(j+1)\,\Delta x$ between times $i\,\Delta t$ and $(i+1)\,\Delta t$ normalized by the duration Δt.

If a given vehicle with identification number id_0 crosses $(j+1)\,\Delta x$ between time $i\Delta t$ and time $(i+1)\,\Delta t$, then id_0 is present in the bucket $[i\,\Delta t,\,(i+1)\,\Delta t]\times[j\,\Delta x,\,(j+1)\,\Delta t]$ and the bucket $[i\,\Delta t,\,(i+1)\,\Delta t]\times[(j+1)\,\Delta x,\,(j+2)\,\Delta t]$. Therefore, $card\left(\{id\,(trace) \mid trace \in bucket_{i,j}\} \cap \{id\,(trace) \mid trace \in bucket_{i,j+1}\}\right)$ is the number of vehicles that have crossed the coordinate $(j+1)\,\Delta x$ in that interval of time. This gives another estimator of the flux based on counting cars in a straightforward way:

$$\widehat{q}_{i,j}^{count} = \frac{1}{n_{lanes}\Delta t}\, card\left(\{id\,(trace) \mid trace \in bucket_{i,j}\} \cap \{id\,(trace) \mid trace \in bucket_{i,j+1}\}\right)$$

1.2.2   Choosing the number of bins

The discretization grid is $\{[i\,\Delta t,\,(i+1)\,\Delta t]\times[j\,\Delta x,\,(j+1)\,\Delta t] \mid (i,j)\in\{1\dots N\}\times\{1\dots N\}\}$. As the estimation formulae above rely on averaging, having a comfortable number of points in each bin provides more stable estimates. It is worth mentioning that usual Central Limit theorem based reasoning for convergence of such estimates is flawed as several samples may correspond to the same vehicle or interacting vehicles, therefore violating the independence assumption of the theorem. Proving the convergence of the estimates above lies clearly beyond the scope of this article and therefore, as a rule of thumb we choose a setup that guarantees that most buckets will host more than 500 traces. This is achieved with a 80×80 grid where the 10th percentile of the number of traces in a given bin is 485. Such a grid also yields a 10th percentile of 58 distinct vehicles per bin. The histograms of number of traces and vehicle per bucket are represented on Figure 2.
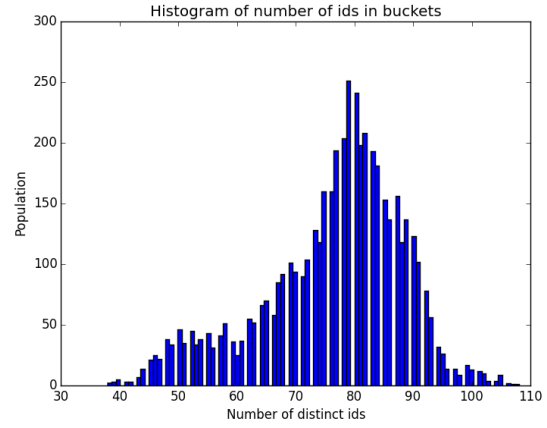
1.2.3   Sanity check for the estimators

This article does not provide any theoretical proof of the convergence of the binned estimators for (v,ρ,q) presented above. It is nonetheless possible to check practically that the procedure is coherent. Two estimators are provided for q that use radically different techniques. The first one relies on the average measured speed and the number of traces in a bin. The other one on counting vehicles transiting from a cell to another. Verifying that they both give similar results for a given bucket will therefore confirm that these estimators for q are trustworthy. It will also certify that the estimation technique for ρ is valid. As one can observe on Figure 3, the scatter plot of $\widehat{q}_{i,j}^{count}$ is plotted against $\widehat{q}_{i,j}$ coincides almost perfectly with the line $y = x$ therefore validating the overall binning and estimation procedure.

1.3   Estimated values for (v,q)

In order to check how well the linearized ARZ model fits actual data, one choses a bounded domain and compares the theoretical solution given by the second order model and the data observed. Here we focus one the values of
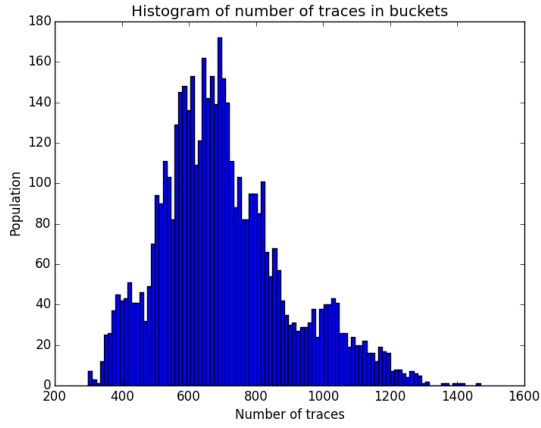
Histogram of number of traces per bucket   Histogram of number of distinct vehicles per bucket

Figure 2: Choice motivation for a 80×80 bucket based discretization grid for the NGSIM data
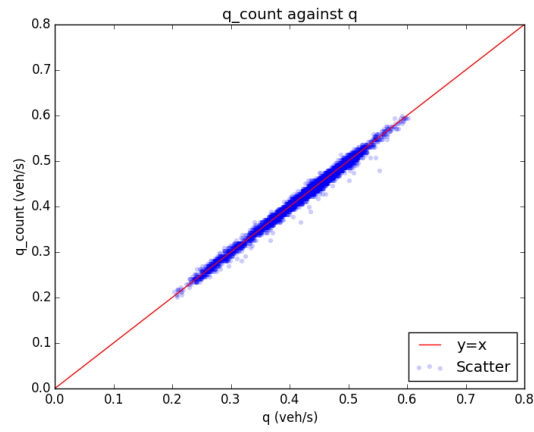

Figure 3: Sanity check for the estimation procedure. $\widehat{q}_{i,j}^{count}$ is plotted against $\widehat{q}_{i,j}$ across the grid of buckets.
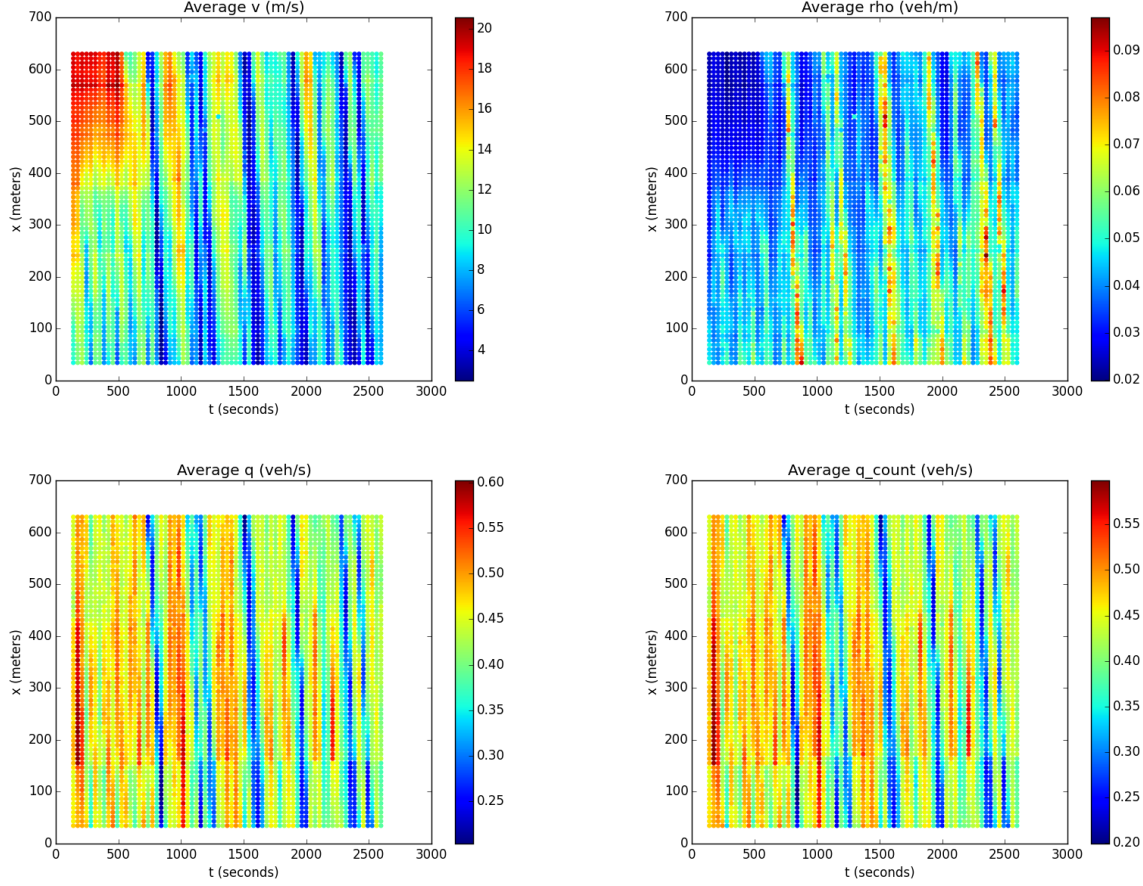
Figure 4: Estimated values for (v, q, ρ). Top left: $\widehat{v}_{i,j}$. Top right: $\widehat{\rho}_{i,j}$. Bottom left: $\widehat{q}_{i,j}$. Bottom right: $\widehat{q}_{i,j}^{count}$.

v and q as they correspond to the setup that is the most worth studying. It is also the most directly practical for control. Now that estimates of the actual values of v and q have been designed, they will be used to compute fundamental diagrams and mapped on the $[0, T] \times [0, L]$ domain. Fundamental diagrams will then yield estimates of the eigen values λ_1 and λ_2 that are crucial in this study. Finally, predicted values of v and q will be compared to their measured counterparts which will allow the computation of a fit error. Based on the estimation of this error for different values of the parameter τ, the value offering the smallest error will be used as an estimate. Plotting maps of both the predicted values and the observed one will also highlight the phenomena the linearized model accounts for and those it cannot characterize.

1.3.1   Maps

Once the values $\widehat{v}_{i,j}$, $\widehat{\rho}_{i,j}$, $\widehat{q}_{i,j}$, $\widehat{q}_{i,j}^{count}$ have been computed they can be plotted on the discretization grid (see Figure 4). As $\widehat{q}$ and $\widehat{q}^{count}$ give extremely similar results, $\widehat{q}^{count}$ will be used as the estimator of q from now on. The estimated values vary in a very smooth manner which corroborates their being well estimated and corresponding to the time domain solution of the linearized ARZ model (see 1.5). However, high flux clusters appearing at the center of the $[0, T] \times [0, L]$ domain clearly contradict the exponential decay along the characteristic lines that is prescribed by the linearized model. Persistent oscillation and smoothly decaying values along characteristic lines are mostly observed outside of these anomalies which clearly coincides with the theoretical predictions of the framework that has been developed above.

1.3.2   Fundamental diagrams

From the values that have been estimated it is very straightforward to compute fundamental diagrams as on Figure 5. One of the potential flaws of studying these fundamental diagrams and using them to calibrate the model's parameters as we do below could come from the fact that the data set is small. Even though many points are
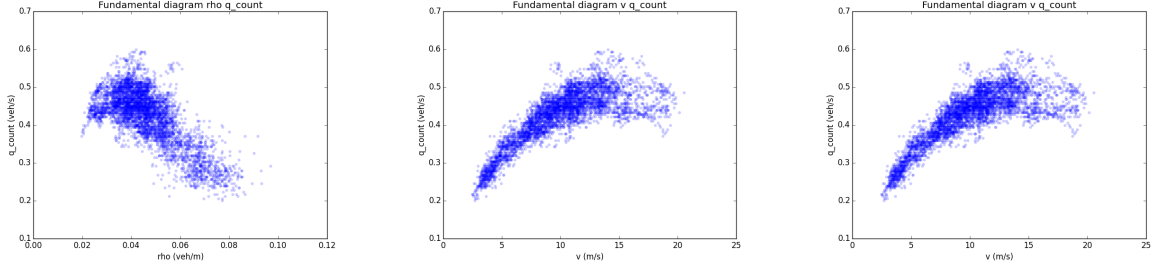
4

Figure 5: Empirical fundamental diagrams. Left: $(\widehat{\rho}, \widehat{q}^{count})$. Middle: $(\widehat{v}, \widehat{q}^{count})$. Right: $(\widehat{\rho}, \widehat{v})$.

collected, they only give information about cars traveling in a small region of time and space. Therefore it is certain that our measurements and estimations are highly correlated. This seems to be confirmed by the fact that the fundamental diagrams below only correspond to the congested regime. Most of the points are concentrated about the same region. This is not enough to guarantee that the estimated quantities are reliable. However, NGSIM is to this day one of the most comprehensive data sets of vehicle behavior on a freeway. It is therefore one of the best ways one has to validate that a traffic model is realistic. The fact that most points lie in the same region is however a sign that the linearization hypothesis is reasonable in that context. Observed deviations from the equilibrium are indeed small. (The equilibrium, i.e. the linearization point, is estimated below).

1.3.3 Calibration of λ_1 and λ_2, linearization point

$\lambda_1 = v^*$ and $\lambda_2 = Q'(v^*)$ therefore the calibration of λ_1 consists in finding a value of v around which the fundamental diagram (v, q) will be linearized. λ_2 will consist in the estimated slope of the fundamental diagram. λ_2 is estimated with a standard Ordinary Least Squares method. The data set above only corresponds to the congested regime and the fundamental diagram is almost affine.
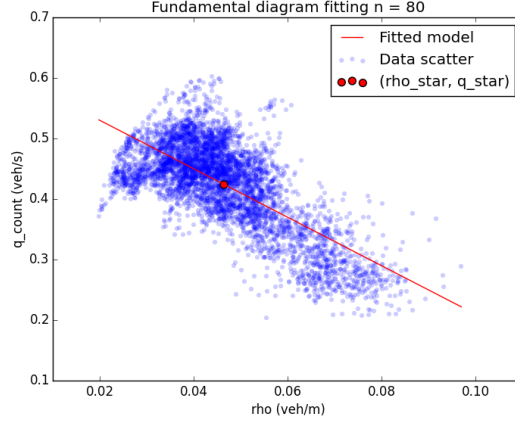
The method used here is therefore quite straightforward. The estimator for v^* is chosen as the empirical mean of $\widehat{v}_{i,j}$: $\widehat{\lambda}_1 = \widehat{v}^*$. A linear model is fitted: $\widehat{q}^{count} = b_1 \widehat{v} + b_0 + \varepsilon$ (where ε represents the noise in the model that would ideally be centered, homoschedastic and uncorrected but is not practically) and the estimator for λ_2 is then $\widehat{\lambda}_2 = \widehat{b}_1$. q^* is estimated by the empirical average of $\widehat{q}^{count}$ and ρ^* by the ratio of the estimates for q^* and v^*. Provided each estimator is convergent, the continuity of the functional $(x, y) \to \frac{x}{y}$ on its domain guarantees the convergence of the estimator for ρ^*. The empirical results for are presented on Figure 6. The determination coefficient is rather mediocre, it could be improved by filtering out outliers and more generally by gathering more data. Improving the quality of the estimation will be the subject of further work on that matter. Significance tests for the coefficients of the linear model are not presented. The assumptions they rely on about the linear depency between $\widehat{q}$ and $\widehat{v}$ are clearly not respected here as the noise is auto-correlated. Again, further work needs to turn this rather heuristic method for estimating parameters into a fully justified statistical procedure. This article focuses is qualitatively assessing what phenomena can be accounted for by the linearized second order model.

1.4 Simulated values for (v, q, ρ)

The data above shows that only the congested regime is to be modeled for the NGSIM data. Therefore the theory developed for the $\lambda_2 < 0$ will be put to use here.

1.4.1 Fourier decomposition of input for a linear PDE

The Partial Differential Equation under scrutiny here is linearized. Therefore, decomposing boundary conditions into a sum and then adding the predicted values inside the domain $[0, T] \times [0, L]$ will give the exact solution. The spectral domain analysis presented above is very useful to that end and will be leveraged thanks to Fourier analysis. Fourier transform is a linear operator that is practically implemented thanks to the Fast Fourier Transform. A real signal $\{f(t) \mid t \in [0, T]\}$ on one of the boundaries $\{(x = 0, t) \mid t \in [0, T]\}$ or $\{(x = L, t) \mid t \in [0, T]\}$ is transformed into a periodic signal by infinite duplication and then turned into a Fourier series $\{t \to \mu + \sum_{k=1}^{n} \beta_k \cdot \cos(k \cdot wt + \phi_k) H \mid t \in [0, T]\}$. This process is known to be convergent with an infinite sum for any square integrable function. It is practically extremely accurate in our case even though the FFT only relies on a finite number of Fourier coefficients. For

Figure 6: Calibration of λ_1 and λ_2. The figure shows the average point used to compute $\widehat{v}^*$ and $\widehat{q}^*$. The affine model used to estimate λ_2 is also plotted.

$$\widehat{\lambda}_1 = 10.07 \quad \widehat{\lambda}_2 = -4.00 \quad \widehat{\rho}^* = 0.04 \quad \widehat{v}^* = 10.07 \quad \widehat{q}^* = 0.42 \quad r^2 = 0.51$$

both upstream and downstream boundary conditions, eye inspection cannot distinguish the original signal from its Fourier series decomposition. In Appendix 1.6 the generic way of computing the solution of the PDE inside the inner domain is presented. The process is quite straightforward although the necessary computations are somewhat cumbersome.

1.4.2 Simulated maps

Prior to using Fourier decomposed signals and elementary solutions, it is necessary to convert the data into the diagonalized basis. First of all, the difference with respect to the equilibrium is computed for each bucket: $\widehat{\widetilde{v}}_{i,j} = \widehat{v}_{i,j} - \widehat{v}^*$, $\widehat{\widetilde{q}}_{i,j} = \widehat{q}_{i,j} - \widehat{q}^*$. Once λ_1 and λ_2 have been estimated, estimates for ξ_1 and ξ_2 are computed thanks to the following equations: $\widehat{\xi}_{1_{i,j}} = \frac{\widehat{\rho}^* \widehat{\lambda}_2}{\widehat{\lambda}_1 - \widehat{\lambda}_2} \widehat{\widetilde{v}}_{i,j} + \widehat{\widetilde{q}}_{i,j}$, $\widehat{\xi}_{2_{i,j}} = \frac{\widehat{\rho}^* \widehat{\lambda}_1}{\widehat{\lambda}_1 - \widehat{\lambda}_2} \widehat{\widetilde{v}}_{i,j}$. Then the predicted values for q and v can be computed thanks to the inverse linear transform $\widetilde{q} = \xi_1 - \frac{\lambda_1}{\lambda_2} \xi_2$, $\widetilde{v} = \frac{\lambda_1 - \lambda_2}{\rho^* \lambda_1} \xi_2$. This procedure gives comparison maps for the data and predicted values for both the (v, q) and the (ξ_1, ξ_2) domains. Figure 7 shows important qualitative properties of the model. First of all, as expected, the model generally predicts with a very good accuracy the decay of all quantities along their characteristic lines. This is a realistic feature that cannot be paralleled by first order models. However, irregularities such as surges of flux at the center of some characteristic lines cannot correspond to the linearized ARZ model in any way. This is a limitation of the model. On this data set, such abnormal regions create fitting errors whose order of magnitude is that of the maximum observed values over the data, therefore the realism of the linearized PDE is very poor for such phenomena. What causes these surges of flux to appear is clearly a compelling question. Exploring it will be the subject of further research that could give rise to new models featuring such turbulent behaviors. The value of τ used to compute the plots below is described in 1.4.3.
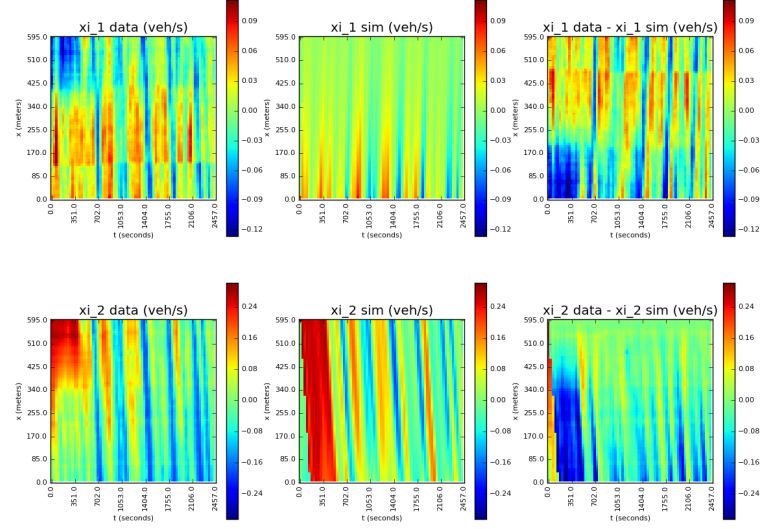
1.4.3 Calibration of τ

For each value of τ one computes the mean absolute error (MAE). That is to say, the average difference in absolute value between what is simulated and what is predicted for each discretization bucket. v and q are not physically homogeneous, therefore it is not sensible to aggregate the errors over these quantities. However, ξ_1 and ξ_2 are both expressed in veh/s. Summing their MAE gives a reliable uni-dimensional index of the quality of the fit with respect to τ. This quantity is computed for different values of τ ranging from 5 to 80 seconds. The value offering the best fit is $\tau^* = 29.68$.

1.5 Time domain explicit resolution of the system

Going back to the diagonalized (v, q) system, it is possible to exhibit an analytical solution. Indeed solving first for $\xi_1(x, t)$ in the PDE $\frac{\partial \xi_1}{\partial t}(x, t) + \lambda_1 \xi_1(x, t) = -\frac{1}{\tau} \xi_1(x, t)$ gives $\xi_1(t, x + \lambda_1 t) = \xi_1(0, t) e^{-\frac{t}{\tau}}$ and re-injecting in $\frac{\partial \xi_2}{\partial t}(t, x) + \lambda_2 \frac{\partial \xi_1}{\partial x}(t, x) = -\frac{1}{\tau} \xi_1(t, x) e^{-\frac{t}{\tau}}$ yields $\xi_2(t, x + \lambda_2 t) = -\frac{1}{\tau} \int_{u=0}^{t} \xi_1(0, x - (\lambda_1 - \lambda_2) u) e^{-\frac{u}{\tau}} du + \xi_2(0, x)$.
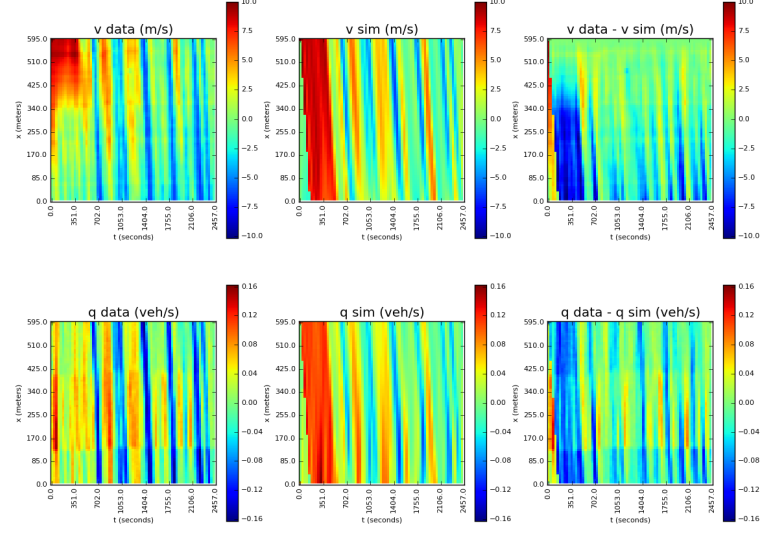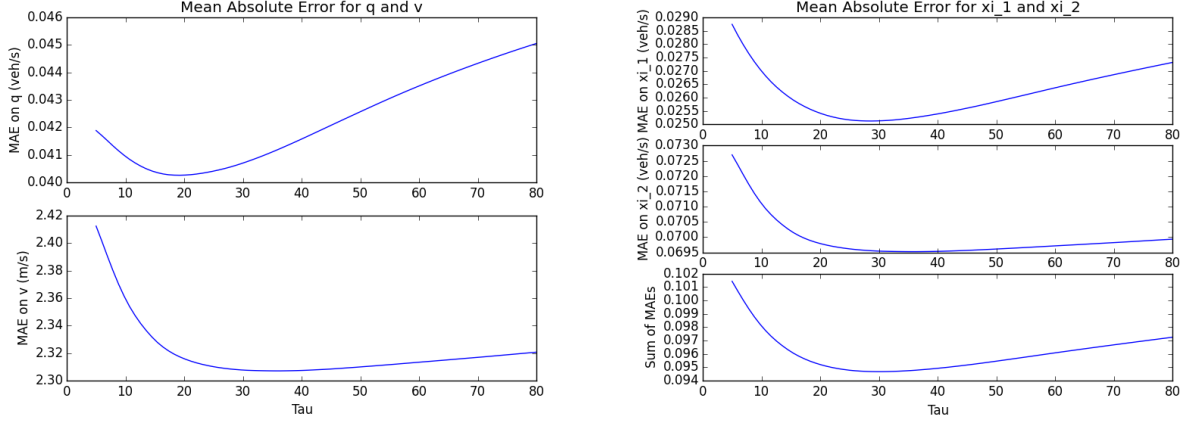
Top row: q. Bottom row: v.

Top row: ξ_1. Bottom row: ξ_2.

Figure 7: Data versus predicted. Top: (v, q) domain. Bottom: (ξ_1, ξ_2) domain. First column: data. Middle column: predictions. Third column: prediction - data.

MAE over q and v	MAE over ξ_1 and ξ_2 and sum of both MAE.

Figure 8: Calibration of τ, one minimizes the sum of MAE over ξ_1 and ξ_2.

1.6 Generic computations for time domain to Laplace domain transforms and vice versa

The aim is to derive the time domain responses of generic input signals such as $t \to H(t)$ and $t \to cos\,(wt + \phi)\,H(t)$ when multiplied in the Laplace domain by $\frac{1}{s+\alpha}$. This then enables the computation of any response that decomposes in a Fourier transform.

1.6.1 Step function input

The time domain input function is $H(t)$. One computes the inverse Laplace transform of $s \to \frac{1}{s(s+\alpha)}$ which is

$$t \to \frac{1}{\alpha}\left(1 - e^{-\alpha t}\right) H(t)$$

1.6.2 Phased cosine input

The time domain input function is $cos\,(wt + \phi)\,H(t)$. One computes the inverse Laplace transform of $s \to \frac{1}{s+\alpha}\left\{\frac{s}{s^2+\omega^2}cos\,(\phi) - \frac{w}{s^2+w^2}sin\,(\phi)\right\}$ which can be directly achieved in the time domain. Indeed, the result is given by the convolution product $t \to \left(e^{-\alpha\cdot}H(\cdot) \star cos\,(\omega \cdot + \phi)\,H(\cdot)\right)(t)$, that is to say

$$t \to \frac{-e^{-\alpha\cdot t}\left(\alpha \cdot cos\,(\phi) + w \cdot sin\,(\phi)\right) + \alpha \cdot cos\,(wt + \phi) + w \cdot sin\,(wt + \phi)}{\alpha^2 + w^2} H(t) = \kappa^{cos}_{\alpha,w,\phi}(t)$$

1.6.3 Fourier sum input

Let the input be $t \to \mu H(t) + \sum_{k=1}^{n} \beta_k \cdot cos\,(k \cdot wt + \phi_k)\,H(t)$. The time domain response is therefore

$$t \to \frac{\mu}{\alpha}\left(1 - e^{-\alpha t}\right) H(t) + \sum_{k=1}^{n} \beta_k \cdot \kappa^{cos}_{\alpha,w,\phi}(t)$$

1.7 Fourier decomposition and time domain responses for $\lambda_2 > 0$

Let $\alpha = -\frac{\lambda_2}{\tau(\lambda_1 - \lambda_2)} < 0$. Let $H(t)$ the Heaviside function.

$$\left(\begin{array}{c} \widehat{\xi}_1(x,s) \\ \widehat{\xi}_2(x,s) \end{array}\right) = \Phi(x,s) \left(\begin{array}{c} \widehat{\xi}_1(0,s) \\ \widehat{\xi}_2(0,s) \end{array}\right)$$

with

$$\Phi(x,s) = \left[\begin{array}{cc} e^{-\frac{sx}{\lambda_1}}e^{-\frac{x}{\lambda_1 \tau}} & 0 \\ -\alpha\frac{\lambda_1}{\lambda_2}\left(e^{-\frac{sx}{\lambda_1}}e^{-\frac{x}{\lambda_1 \tau}} - e^{-\frac{sx}{\lambda_2}}\right)\frac{1}{s+\alpha} & e^{-\frac{sx}{\lambda_2}} \end{array}\right]$$

8

implies the following fundamental responses for the system.

1.7.1 Fundamental responses in time domain:

- $\begin{pmatrix} \xi_1(0,t) \\ \xi_2(0,t) \end{pmatrix} = \begin{pmatrix} H(t) \\ 0 \end{pmatrix}$:

  - $\xi_1(x,t) = e^{-\frac{x}{\lambda_1 \tau}} H\left(t - \frac{x}{\lambda_1}\right)$

  - $\xi_2(x,t) = -\frac{\lambda_1}{\lambda_2}\left(e^{-\frac{x}{\lambda_1 \tau}}\left(1 - e^{-\alpha\left(t - \frac{x}{\lambda_1}\right)}\right) H\left(t - \frac{x}{\lambda_1}\right) - \left(1 - e^{-\alpha\left(t - \frac{x}{\lambda_2}\right)}\right) H\left(t - \frac{x}{\lambda_2}\right)\right)$

- $\begin{pmatrix} \xi_1(0,t) \\ \xi_2(0,t) \end{pmatrix} = \begin{pmatrix} 0 \\ H(t) \end{pmatrix}$:

  - $\xi_1(x,t) = 0$

  - $\xi_2(x,t) = H\left(t - \frac{x}{\lambda_2}\right)$

- $\begin{pmatrix} \xi_1(0,t) \\ \xi_2(0,t) \end{pmatrix} = \begin{pmatrix} \cos(\omega t + \phi) \\ 0 \end{pmatrix}$:

  - $\xi_1(x,t) = e^{-\frac{x}{\lambda_1 \tau}} \cos\left(\omega\left(t - \frac{x}{\lambda_1}\right) + \phi\right) H\left(t - \frac{x}{\lambda_1}\right)$

  - $\xi_2(x,t) = -\frac{\lambda_1 \alpha}{\lambda_2}\left(e^{-\frac{x}{\lambda_1 \tau}} \kappa^{cos}_{\alpha,\omega,\phi}\left(t - \frac{x}{\lambda_1}\right) - \kappa^{cos}_{\alpha,\omega,\phi}\left(t - \frac{x}{\lambda_2}\right)\right)$

- $\begin{pmatrix} \xi_1(0,t) \\ \xi_2(0,t) \end{pmatrix} = \begin{pmatrix} 0 \\ \cos(\omega t + \phi) \end{pmatrix}$:

  - $\xi_1(x,t) = 0$

  - $\xi_2(x,t) = \cos\left(\omega\left(t - \frac{x}{\lambda_2}\right) + \phi\right) H\left(t - \frac{x}{\lambda_2}\right)$

1.8 Fourier decomposition and time domain responses for $\lambda_2 < 0$

This time, $\alpha = -\frac{\lambda_2}{\tau(\lambda_1 - \lambda_2)} > 0$.

$$\begin{pmatrix} \widehat{\xi_1}(x,s) \\ \widehat{\xi_2}(x,s) \end{pmatrix} = \Phi(x,s) \begin{pmatrix} \widehat{\xi_1}(0,s) \\ \widehat{\xi_2}(L,s) \end{pmatrix}$$

with

$$\Gamma(x,s) = \begin{pmatrix} e^{-\frac{sx}{\lambda_1}} e^{-\frac{x}{\lambda_1 \tau}} & 0 \\ \alpha\frac{\lambda_1}{\lambda_2}\left(e^{-\frac{x}{\lambda_1 \tau}} e^{-\frac{sx}{\lambda_1}} - e^{-\frac{L}{\lambda_1 \tau}} e^{-\frac{s}{\lambda_2}\left(x - L\frac{\lambda_1 - \lambda_2}{\lambda_1}\right)}\right)\frac{1}{s + \alpha} & e^{-\frac{s(x-L)}{\lambda_2}} \end{pmatrix}$$

implies the following fundamental responses for the system.

1.8.1 Fundamental responses in time domain

- $\begin{pmatrix} \xi_1(0,t) \\ \xi_2(L,t) \end{pmatrix} = \begin{pmatrix} H(t) \\ 0 \end{pmatrix}$:

  - $\xi_1(x,t) = e^{-\frac{x}{\lambda_1 \tau}} H\left(t - \frac{x}{\lambda_1}\right)$

  - $\xi_2(x,t) = \frac{\lambda_1}{\lambda_2}\left(e^{-\frac{x}{\lambda_1 \tau}}\left(1 - e^{-\alpha\left(t - \frac{x}{\lambda_1}\right)}\right) H\left(t - \frac{x}{\lambda_1}\right) - e^{-\frac{L}{\lambda_1 \tau}}\left(1 - e^{-\alpha\left(t - \frac{x - L\frac{\lambda_1 - \lambda_2}{\lambda_1}}{\lambda_2}\right)}\right) H\left(t - \frac{x - L\frac{\lambda_1 - \lambda_2}{\lambda_1}}{\lambda_2}\right)\right)$

9

- $\begin{pmatrix} \xi_1\left(0,t\right) \\ \xi_2\left(L,t\right) \end{pmatrix} = \begin{pmatrix} 0 \\ H\left(t\right) \end{pmatrix}$:

    - $\xi_1\left(x,t\right) = 0$
    - $\xi_2\left(x,t\right) = H\left(t - \frac{x-L}{\lambda_2}\right)$

- $\begin{pmatrix} \xi_1\left(0,t\right) \\ \xi_2\left(L,t\right) \end{pmatrix} = \begin{pmatrix} \cos\left(\omega t + \phi\right) \\ 0 \end{pmatrix}$:

    - $\xi_1\left(x,t\right) = e^{-\frac{x}{\lambda_1 \tau}} \cos\left(\omega\left(t - \frac{x}{\lambda_1}\right) + \phi\right) H\left(t - \frac{x}{\lambda_1}\right)$
    - $\xi_2\left(x,t\right) = \frac{\lambda_1 \alpha}{\lambda_2}\left(e^{-\frac{x}{\lambda_1 \tau}} \kappa_{\alpha,\omega,\phi}^{cos}\left(t - \frac{x}{\lambda_1}\right) - e^{-\frac{L}{\lambda_1 \tau}} \kappa_{\alpha,\omega,\phi}^{cos}\left(t - \frac{x - L\frac{\lambda_1 - \lambda_2}{\lambda_1}}{\lambda_2}\right)\right)$

- $\begin{pmatrix} \xi_1\left(0,t\right) \\ \xi_2\left(L,t\right) \end{pmatrix} = \begin{pmatrix} 0 \\ \cos\left(\omega t + \phi\right) \end{pmatrix}$:

    - $\xi_1\left(x,t\right) = 0$
    - $\xi_2\left(x,t\right) = \cos\left(\omega\left(t - \frac{x-L}{\lambda_2}\right) + \phi\right) H\left(t - \frac{x-L}{\lambda_2}\right)$